Scientific Research Publishing

Open Journal of Metal, 2018, 8, 15-33
http://www.scirp.org/journal/ojmetal
ISSN Online: 2164-277X
ISSN Print: 2164-2761

Effect of Deformation during Stamping on Structure and Property Evolution in 3rd Generation AHSS

Daniel Branagan[1], Craig Parsons[2], Tad Machrowicz[2], Jonathon Cischke[2], Andrew Frerichs[1], Brian Meacham[1], Sheng Cheng[1], Grant Justice[1], Alla Sergueeva[1]

[1]The NanoSteel Company, Idaho Falls, ID, USA
[2]The NanoSteel Company, Troy, MI, USA
Email: dbranagan@nanosteelco.com

How to cite this paper: Branagan, D., Parsons, C., Machrowicz, T., Cischke, J., Frerichs, A., Meacham, B., Cheng, S., Justice, G. and Sergueeva, A. (2018) Effect of Deformation during Stamping on Structure and Property Evolution in 3rd Generation AHSS. *Open Journal of Metal*, **8**, 15-33.
https://doi.org/10.4236/ojmetal.2018.82002

Received: May 9, 2018
Accepted: June 25, 2018
Published: June 28, 2018

Abstract

Over the past decade extensive development of advanced high strength steel (AHSS) was driven by the demand from the automotive industry for stronger materials that can enable lightweighting to meet increasing fuel efficiency requirements. However, achievement of higher strength in many AHSS grades comes with reductions in ductility, leading to geometric constraints on formability and limiting their application. In this paper, a 3rd Generation AHSS with a compelling property combination of high tensile strength of ~1200 MPa and total elongation > 40% was used for laboratory and stamping studies. Various auto related laboratory tests were done including tensile testing, 180 degree bending, bulge testing, and cup drawing to estimate the steel's formability under different applied conditions. Additionally, since laboratory testing provides only an estimation of the potential stamping response, the 3rd Generation AHSS sheet was stamped into B-pillars under industrial stamping conditions. Non-destructive and destructive analysis of the resulting stampings were done to evaluate the microstructural and property changes occurring during stamping. Significant strengthening of material in the stamped part is attributed to the structural changes through the complex Nanophase Refinement and Strengthening mechanism.

Keywords

Steel, Advanced High Strength Steel, Cold Formability, Stamping, Structure, Properties

1. Introduction

With current market trends and governmental regulations pushing towards

higher efficiency in vehicles, AHSS are increasingly being pursued for their ability to provide reductions in gauge thickness compensated by higher strength [1] [2] [3] [4] [5]. One of the biggest obstacles to using high strength steel sheets for automobile body components, to reduce weight and improve safety, are the issues related to limited formability. Different aspects of AHSS cold formability and related issues are widely discussed in various publications [6] [7] [8] [9]. Thus, improved formability of steel is enabling the design of more complex part geometries facilitating the desired weight reduction for automotive applications.

Formability may be broken into two distinct forms: local formability and bulk formability [9]. Local formability provides the ability for an edge (or tight radius) to be formed into a certain shape. Edges, which may occur in internal holes or external free surfaces may have reduced ductility due to the presence of defects such as cracks or structural changes resulting from the creation of the sheet edge. Edge formability is often measured using hole expansion ratio testing with holes put into the material by various methods including punching, laser cutting, milling, and wire-EDM. Bulk formability is dominated by the intrinsic ductility under both simple and complex stress states and may be affected by deformation pathway and the strain rate occurring during deformation. Bulk formability can be measured by a variety of methods under specific stress states with results often summarized in a forming limit diagram.

The World Auto Steel "banana plot" represents the trends of new steel development and the resulting paradox of strength and ductility [10]. The general trends are that increases in strength results in a reduction of ductility, which in turn is expected to lead to limited formability of sheet material during stamping operations. In March 2016, NanoSteel commercially launched a non-stainless 3rd Generation AHSS and in this paper, industrial produced blanks of NXG™ 1200 will be utilized for laboratory testing and industrial stamping [11] [12] [13] [14] [15]. An example of the engineering tensile stress-strain curve for the sheet material tested in accordance with ASTM E8 standard [16] is shown in **Figure 1(a)**. At the top of **Figure 1(b)**, the tensile specimen corresponding to the engineering stress-strain curve in **Figure 1(a)** is shown before and after testing. A close-up view of the break area of the tensile specimen is provided at the bottom of **Figure 1(b)**. As can be seen, the sample failure occurred with a typical ~45˚ breakage and deformation bands parallel and perpendicular to the breakage are visible on the sample surface. In the sample shown, dynamic strain aging (DSA) is found to occur commensurate with the serrations on the stress-strain curve (**Figure 1(a)**). The nature of the deformation bands, their dependence on strain rate and stress state has been described in detail previously [17].

In **Figure 1(c)**, a true stress-true strain tensile curve corresponding to the engineering stress-strain curve shown in **Figure 1(a)** is provided. Additionally, incremental tensile testing curves measured in 4% strain increments with the specimen gauge re-measured manually between tests are graphed on the same plot. The stress–strain curves from each incremental testing plotted together

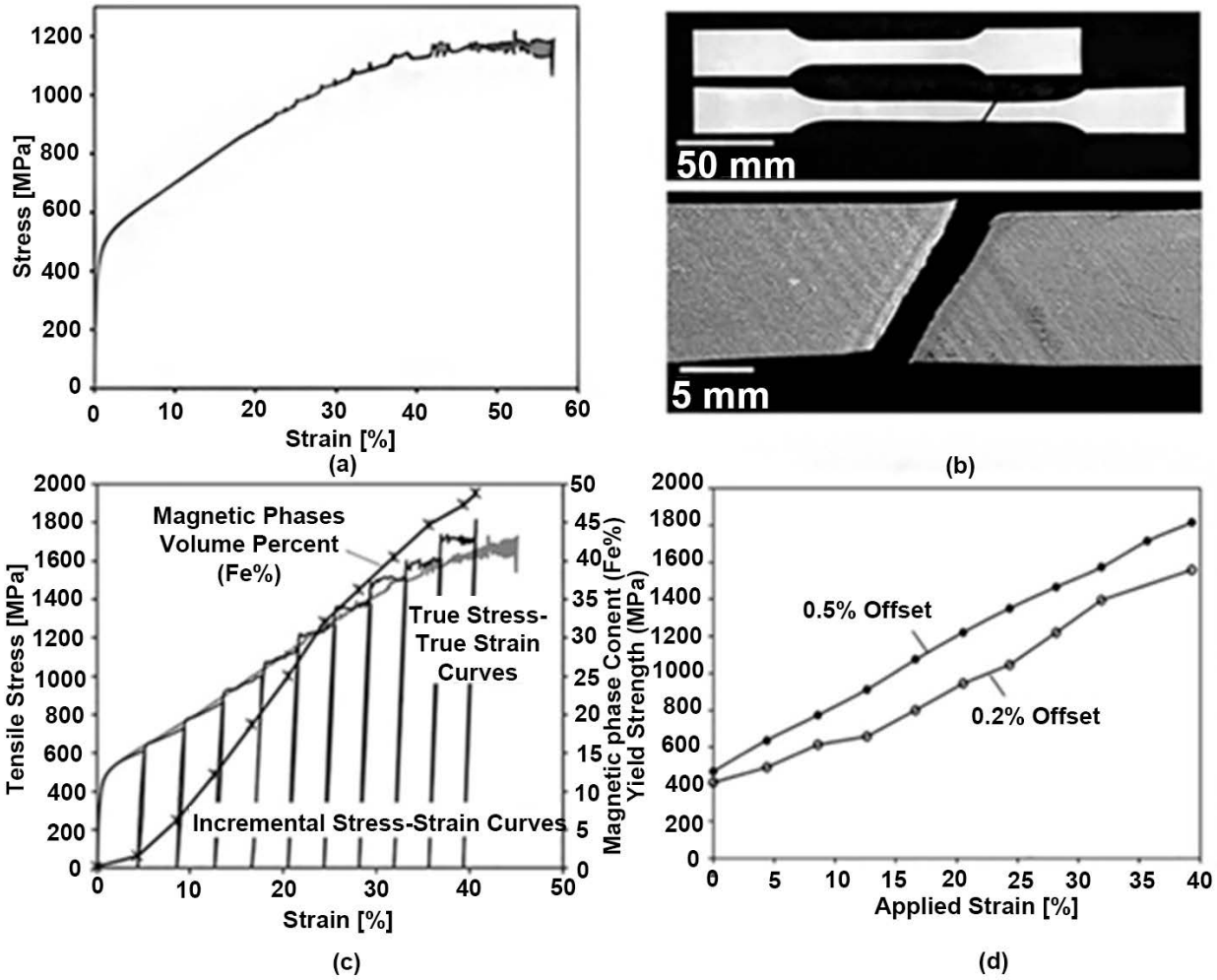

Figure 1. (a) Engineering stress-strain tensile curve of NXG™ 1200, (b) corresponding ASTM E8 tensile specimen before and after testing (top image) and close-up view of the break in the tensile specimen illustrating presence of deformation bands (bottom image), (c) true stress–true strain tensile curve, incremental tensile testing curves, and magnetic phases volume percent (Fe%) at each strain increment, and (d) yield strength as a function of applied strain.

follow closely the calculated true stress–true strain curve with slight deviation at high strain levels affected by localized strengthening in deformation bands. After each test, the gauge section of the sample was analyzed with a Feritscope and the total magnetic phases volume percent (Fe%) is additionally shown. Note that the Feritscope uses a magnetic induction technique whereby the applied field in the probe interacts with the volume magnetization in the sample. Thus the data is reported as total magnetic phases volume percent since this technique does not distinguish between different magnetic phases such as alpha-ferrite and alpha-martensite, for example. The maximum value recorded during the testing was 49 Fe%. Figure 1(d), the yield strength as a function of total applied strain is shown with data taken from the recorded incremental tensile testing curves. As the increase in the yield strength clearly shows, the material exhibits a high level of strain hardening and resistance to necking for nearly the full range of tensile ductility.

In this paper, the focus will be on structure and property changes occurring in NanoSteel 3rd Generation AHSS when cold deformed. Results will include studies on laboratory tensile specimens, incremental tensile testing for property evaluation as a function of strain and data from tests commonly used to estimate metal sheet formability including 180 degree bending, bulge testing, and cup drawing. Additionally, results will be included on non-destructive and destructive testing of stampings from industrial produced blanks of NXG™ 1200 and the results will be compared to those generated from laboratory samples.

2. Background

2.1. Structural Changes during Deformation

As shown in the previous section, NXG™ 1200 demonstrates a combination of high strength and ductility reaching 69,400 MPa% in the case of the example tensile curve in **Figure 2(a)**. The microstructure in the 3rd Generation NanoSteel sheet before deformation (*i.e.* 3GNS-BD) corresponding to that in an industrial coil is illustrated by SEM and TEM micrographs in **Figure 2(a)** and **Figure 2(b)**, respectively. The microstructure consists primarily of recrystallized micron-sized austenite grains which can be seen as distinct grains at both magnifications. Additional features on the micrographs are identified as annealing twins and stacking faults. Annealing twins, for example, can be readily seen in the upper right grain of **Figure 2(b)**. Detailed analysis of the structure (not presented here) also reveals a small fraction of ferrite (<1%) and the presence of isolated nanoprecipitates typically in the 5 to 100 nm size range. Note that the nanoprecipitates, which are a strengthening component, were identified as separate phases: structurally, based on electron diffraction analysis, and chemically, based on energy dispersive spectroscopy scans.

During tensile testing to failure, the initial structure (3GNS-BD) undergoes Nanophase Refinement and Strengthening (NR&S) leading to formation of the final structure (3GNS-AD). The NR&S mechanism leading to structural evolution during cold deformation described above involves complex interaction of dislocation dominated deformation mechanisms along with phase transformation, nanoscale phase formation, nanoprecipitation, and dynamic strain aging effects. In-depth information related to the details of this mechanism has been presented recently [17] [18]. In this paper, related to the analysis of metal stampings, the focus will be on the structural changes during forming operations and their correlation with that previously observed during tensile testing, which are described below.

The microstructure of the 3rd Generation NanoSteel sheet after deformation (*i.e.* 3GNS-AD), is demonstrated by the SEM and TEM micrographs in **Figure 2(c)** and **Figure 2(d)**, respectively. Note that the images are taken from the tensile gauge near the fracture. As can be seen, the structure after deformation is much different than the starting structure and consists of two distinct microstructural regions of Microconstituent 1 (labeled 1) and Microconstituent 2 (labeled 2) as shown in **Figure 2(d)**.

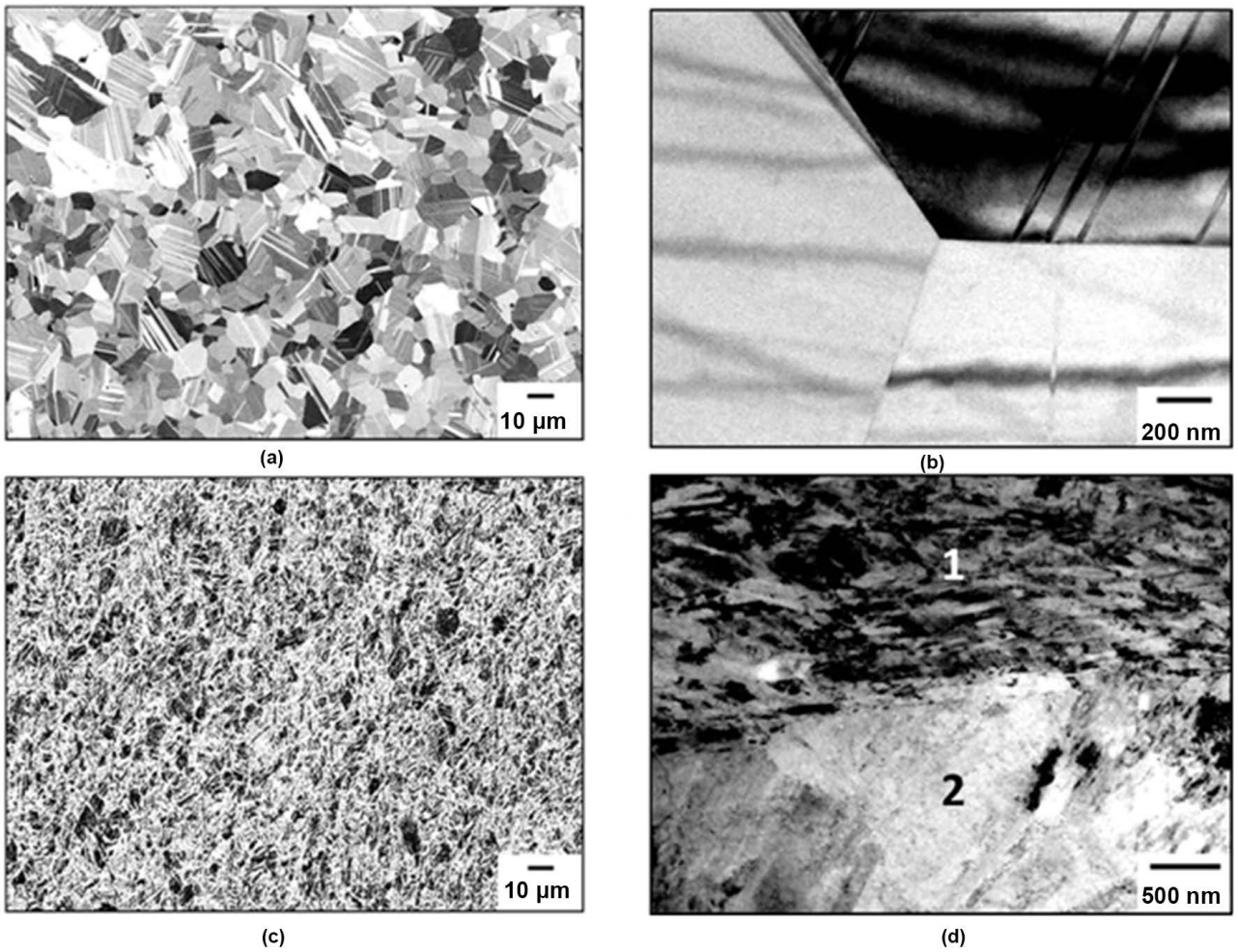

Figure 2. Microstructure in the NXG™ 1200 sheet before and after deformation; (a) SEM back-scattered micrograph of the initial structure before deformation (3GNS-BD), (b) TEM bright-field micrograph of the same initial structure before deformation (3GNS-BD), (c) SEM back-scattered micrograph of the final structure after deformation (3GNS-AD), and (d) TEM bright-field micrograph of the same final structure after deformation (3GNS-AD) showing areas with ferrite (Microconstituent 1) and austenite (Microconstituent 2).

Further details of the 3GNS-AD structure highlighting microstructural features are shown for Microconstituent 1 in **Figure 3** and for Microconstituent 2 in **Figure 4**. Note that the sample studied was deformed in uniaxial tension at a strain rate of 0.0013/s until failure to a total elongation of 56.2%. A TEM bright-field image of the microstructure corresponding to Microconstituent 1 in NXG™ 1200 sheet material is shown in **Figure 3(a)**. Microconstituent 1 is characterized by refined ferrite transformed from austenite and nanoprecipitates. While the austenite to ferrite transformation may indeed be of martensitic type, the formation of nanoprecipitates show that the mechanism is more complex and involves not only pure shear transformation but short range diffusion as well. Examples of the nanoprecipitates are highlighted by black circles in **Figure 3(b)**. Microconstituent 1 is found to contain significant volume fractions of nanoprecipitates, typically from 5 to 20 nm in diameter although larger nanoprecipitates can be occasionally found up to 100 nm in size.

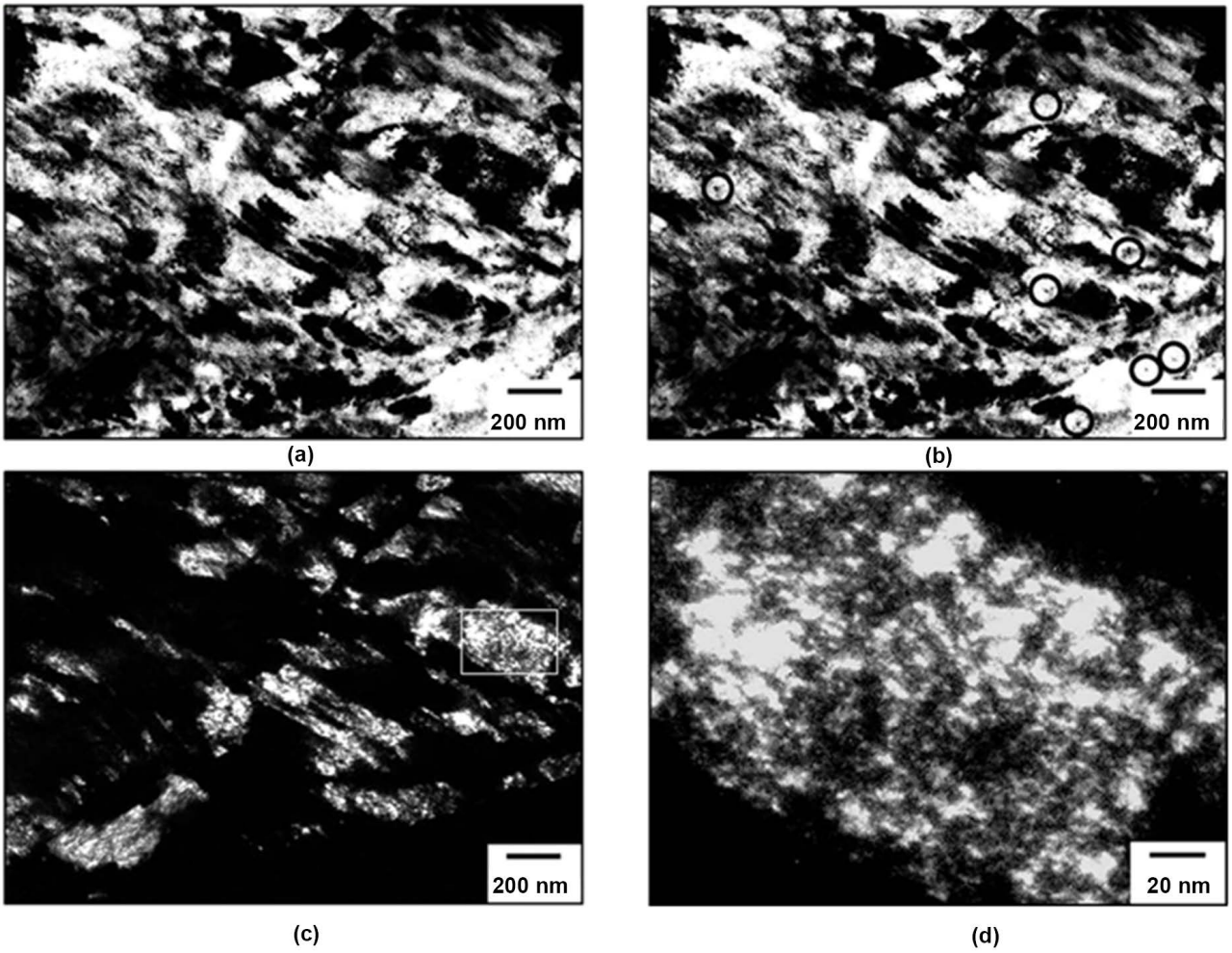

Figure 3. Microconstituent 1 in NXG™ 1200 structure after deformation; (a) TEM bright-field micrograph of Microconstituent 1 area of microstructure represented by ferrite grains and nanoprecipitates, (b) TEM bright-field micrograph with highlighted examples of nanoprecipitates (see black circles), (c) TEM dark-field micrograph showing nanoscale size of the ferrite grains in Microconstituent 1, and (d) high magnification TEM dark-field micrograph showing a selected nanoscale ferrite grain (marked by box in 3c) containing a high density of dislocation tangles.

In **Figure 3(c)**, a TEM dark-field micrograph of the Microconstituent 1 area illustrates the nanoscale size of the ferrite grains that are typically from 150 to 300 nm in size and formed as a result of transformation from austenite during the deformation process. Newly formed nanoscale ferrite grains are also found to participate in the deformation process through dislocation mechanisms. In **Figure 3(d)**, a TEM dark-field micrograph shows a selected nanoscale ferrite grain at higher magnification. As it can be seen, this grain contains a high density of dislocation tangles indicating that after formation, this grain continued to deform and contribute to global plasticity and is an enabling component in achieving the observed ductility (*i.e.* >40% total elongation).

Microconstituent 2 is characterized by the formation of dislocation cells in the austenite grains and concurrent formation of nanoprecipitates. In **Figure 4(a)**, a TEM bright-field micrograph of Microconstituent 2 area is shown where the

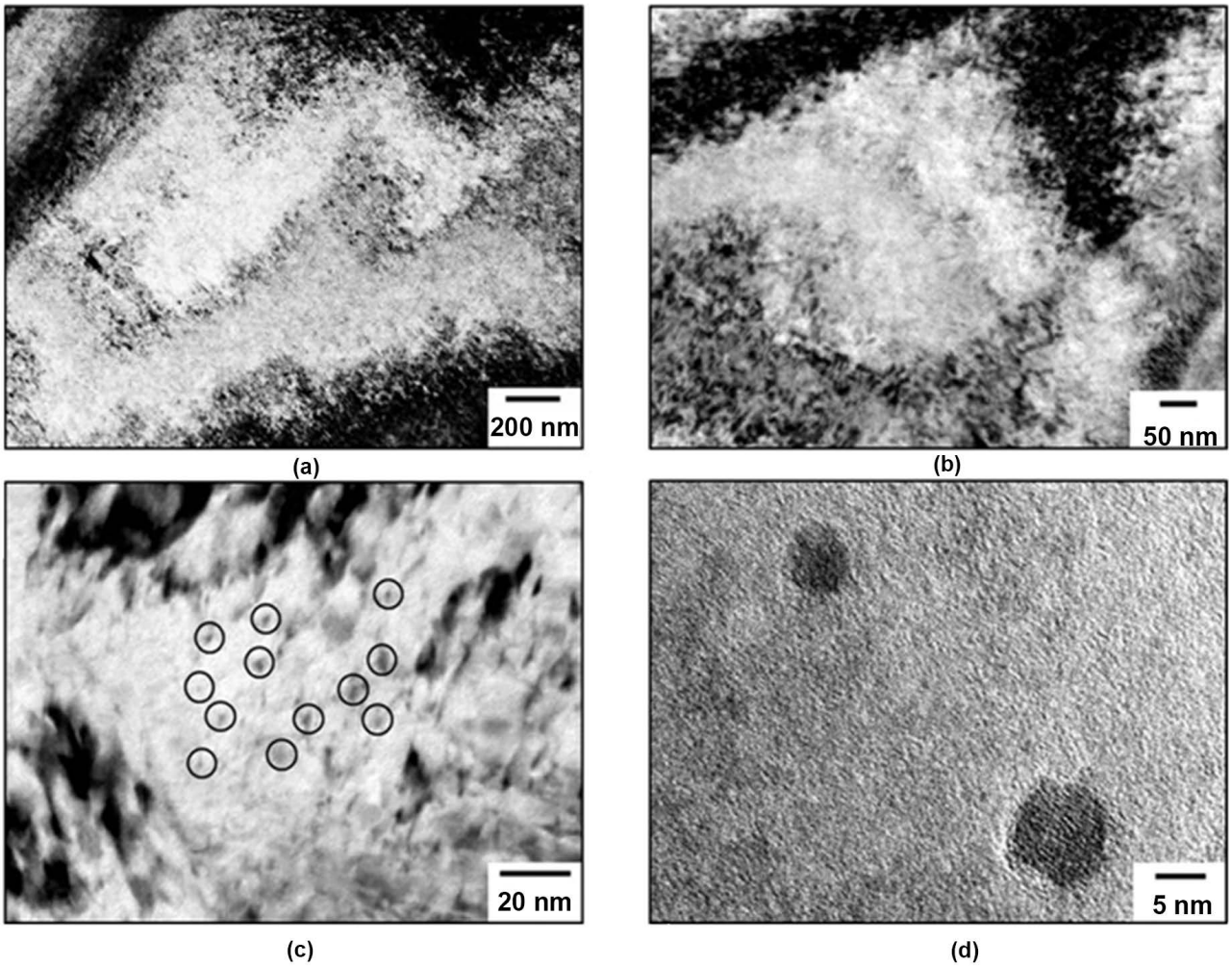

Figure 4. Microconstituent 2 in NXG™ 1200 structure after deformation; (a) TEM bright-field micrograph of Microconstituent 2 area of microstructure represented by micron-sized austenite grains and nanoprecipitates, (b) TEM bright-field micrograph of the deformed austenite grain at higher magnification showing a dislocation cell structure, (c) TEM micrograph highlighting examples of nanoprecipitates (see black circles), and (d) high resolution TEM micrograph illustrating two nanoprecipitates under 10 nm in size.

micron-sized austenite structure can be seen. In these areas, the austenite does not transform during deformation but accumulates a high density of dislocations forming dislocation block boundaries (*i.e.* black regions outlining the grains) and nanoscale cell structures with cell size typically from 10 to 20 nm (*i.e.* the internal structures observed inside the grains). Figure 4(b), a higher magnification TEM bright-field micrograph shows a deformed austenite grain with a fine nanoscale dislocation cell structure. The presence of nanoprecipitates in the austenite grains is highlighted by black circles in Figure 4(c). These nanoprecipitates are found to be typically 5 to 20 nm in size with a volume fraction up to 6 volume percent in the austenitic matrix of Microconstituent 2. In Figure 4(d), a high resolution TEM micrograph illustrates examples of two nanoprecipitates in the deformed material demonstrating their extremely small size under 10 nm.

2.2. Cold Formability during Laboratory Tests

Various laboratory tests can be used to gain an understanding of a material's potential performance upon stamping. A summary of various test results for commercially produced NXG™ 1200 sheet with thickness of 1.4 mm is presented below.

Tensile testing is one of the tests sometimes utilized for cold formability evaluation. Uniaxial tensile testing was performed in accordance with the ASTM E8 standard [16]. **Figure 5(a)** shows typical tensile engineering stress vs. engineering strain curves for samples cut in three different orientations with respect to rolling direction: longitudinal, transverse, and 45˚ diagonal. As it can be seen, similar properties were recorded independently from sample orientation. Uniformity of the properties in different directions with respect to rolling is very important for the material performance at stamping operations, in order to avoid unexpected failures in a part with a complex geometry. In **Figure 5(b)**, a total tensile elongation is plotted as a function of strain rate in a range from 0.0008 s^{-1} to 1200 s^{-1} at tensile testing. As shown, the total elongation until failure remained constant up to 100 s^{-1} strain rate and increases, with at least 8 percent higher, between 100 s^{-1} and 1200 s^{-1}. In recent publication by Kuhlman *et al.* [19] more details provided on strain rate dependence. It was also shown that ductile fracture was observed in all samples tested in the utilized strain rate range [19].

Bendability was evaluated by ISO 7438 guided bend test method with a range of nose diameters down to approximately 0.5 mm. In this method, the specimen is set across two supports and lubricated. The forming nose is pushed downward in the middle of the supports and into the specimen until 180˚ bending occurs or until the sample fails. No cracking was observed in any bend samples down to R/t ratio of 0.34 at a 180° bend and in many samples as low R/t ratio as 0.23 (**Figure 5(c)**).

Drawability was evaluated by drawing full cups from circular blanks with a range of diameters into a die using a cylindrical ram having a 1.9" diameter. During the testing, a blank was centered in the hole of the die and the cylindrical ram was advanced into the die, thereby drawing in the blank. Drawing of the blank progressed until the material had either fully drawn into the die to form a cup, or ruptured. Using this method, the ability of the 1.4 mm gauge sheet to be drawn with draw ratio up to 1.9 without rupture or cracking was demonstrated (**Figure 5(d)**). More details on drawability and resistance to delayed cracking were provided in [20] [21].

Another test to demonstrate formability of the material was mechanical bulge testing utilizing 7" square blanks that were formed using rounded cylindrical ram of 3" in diameter. Samples were bulged until fracture to determine the maximum dome height before rupture. **Figure 5(e)** shows an example of bulge sample after testing that was stopped before failure. Dome heights up to 44.6 mm were recorded for this material.

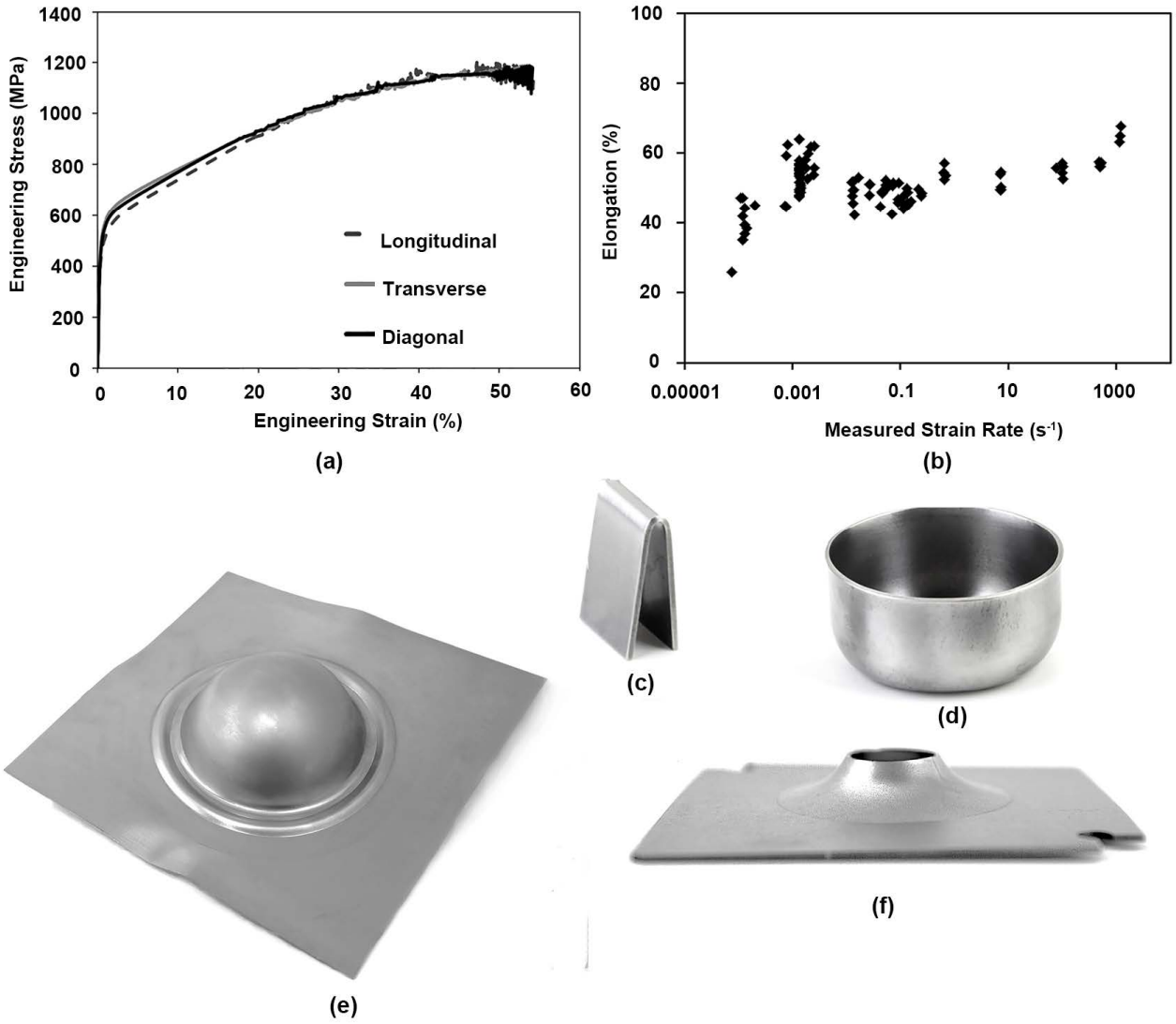

Figure 5. NXG™ 1200 sheet material; (a) example of the directional tensile properties, (b) tensile elongation at a range of strain rates, (c) example of the sample bent to 180 degree with R/t ratio of 0.39, (d) example of the drawn cup with draw ratio of 1.9, (e) example of the sample after bulge testing with dome height of 44.1 mm, and (f) example of the sample after hole expansion with ratio of 46.0%.

Hole expansion testing was used to evaluate edge stretchability of the material. Using samples with punched holes of 10 mm in diameter with punching speed of 228 mm/sec, hole expansion was performed at quasi static ram speed of 50 mm/min. An average hole expansion ratio of 45% was demonstrated (**Figure 5(f)**). By varying the method of hole preparation, punch speed, expansion speed, and/or reversing structural transformation at hole edge, a substantial increase in HER values with up to ≥140% can be achieved [22] [23] [24].

3. Results

3.1. Cold Formability during Commercial Stamping

As shown in the background section, based on the laboratory results, including

tensile testing, 180 degree bending, bulge testing, and cup drawing indicated that NanoSteel 3rd Generation AHSS should exhibit good cold formability during cold stamping. To test this assumption, samples of sheet from commercially produced coil with tensile properties provided in Figure 5(a) were used for B-pillar stamping trial at a commercial stamping facility with stamping speed estimated at 290 mm/s. Using an existing die, NXG™ 1200 sheet was stamped into a B-pillar progressively through 4 stages without issues. Note that the blank was put into the die while cold and no external heating was applied. Die temperature and temperature rise from the adiabatic heating during deformation was not measured in this study. Signs of localized thinning/necking even in areas between the expanded holes were not observed (see Figure 6(c)). The structure and properties of the material in the stamped part were examined in detail.

3.2. Non-Destructive Evaluation of Stamped Part

Feritscope measurements provide an indication of the structural changes occurring during deformation from stamping. As shown previously, in the NXG™ 1200 sheet the initial 3GNS-BD structure changes from paramagnetic austenite to the ferromagnetic ferrite in the 3GNS-AD structure during cold deformation through the NR&S mechanism. Increase in the volume fraction of Microconstituent 1 after deformation results in higher Fe% measured due to the formation of alpha-Fe. Measurements were taken by using a Fisher Feritscope from the stamped B-pillar surface with an ~20 mm grid pattern shown in Figure 6. Grid adjustments were made to hit specific features such as bent surfaces and corners. More than 1500 measurements were taken to essentially scan the entire B-pillar

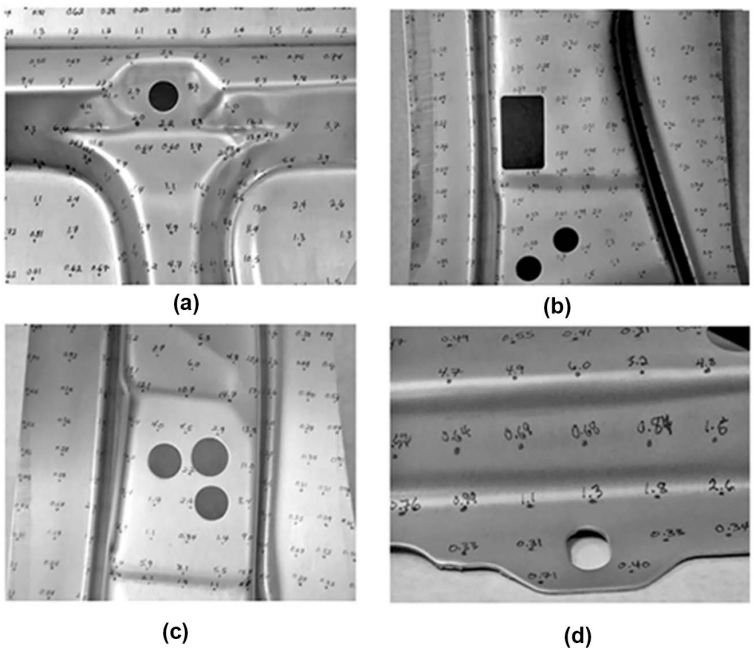

Figure 6. B-pillar surface with ~20 mm grid pattern; (a) top section, (b) middle section 1, (c) middle section 2, and (d) bottom section.

to allow a correlation of non-destructive measurements with the destructive measurements in the next section. Note that the Feritscope uses a small 1.5 mm probe that allows data to be measured even in areas where destructive tensile testing is not possible due to a non-planar geometry. From the Feritscope measurements, Fe% varied in a range from 0.1% to 0.4% Fe% in most flat areas of the B-pillar (same as in the initial sheet before stamping) and up to 31 Fe% in the most deformed areas.

Rockwell C (HRc) hardness measurements were also used as a non-destructive method to evaluate the deformation effect during stamping operation on material structure and properties. However, in contrast to Feritscope measurements, this method is limited to flat surfaces for measurements and cannot provide information on the most deformed curved areas of the B-pillar. The hardness of the sheet before stamping was ~20 HRc. Hardness in a range from 20 to 47 HRc was recorded for the stamped part confirming the strengthening effect from the NR&S mechanism activation during stamping.

3.3. Destructive Evaluation of Stamped Part

For destructive analysis, tensile specimens were cut along the entire length of the B-pillar as shown in **Figure 7(a)** and **Figure 7(b)**. Tensile specimens with a reduced size (*i.e.* 12.5 mm gauge) were used to evaluate material properties in the stamped part [25]. In total, 213 tensile specimens were tested. Tensile testing was done on an Instron mechanical testing frame (Model 5984), utilizing Instron's Bluehill control and analysis software. All tests were run at ambient temperature in displacement control. Samples were tested at a displacement rate of 0.025 mm/s during initial loading to 2% strain and 0.125 mm/s for the remaining duration of the test. Rockwell C hardness and Feritscope measurements were taken from each tensile specimen. Tensile property data for selected specimens are listed in **Table 1**.

Examples of the stress – strain curves for specimens cut from the B-pillar with various levels of magnetic phases volume percent (Fe%) are presented in **Figure 7(c)**. Corresponding true stress-true strain curves in **Figure 7(d)** show extensive strain hardening in the material indicating the effect of NR&S on the sheet structure during stamping. Each specimen showed a rapid decrease in strength after achieving ultimate tensile strength corresponding to necking behavior.

Detailed TEM analysis was done on the samples cut from different locations of the stamped part to demonstrate the structural response to the deformation during stamping. **Figure 8** shows the bright-field TEM images of the microstructure in the selected samples cut from the stamped B-pillar before and after tensile testing.

Selected samples containing 4.6 Fe%, 13.9 Fe%, and 24.5 Fe% after stamping as provided in **Table 1** with corresponding stress-strain curves shown in **Figure 7** were analyzed by TEM. In **Figure 8(a)**, **Figure 8(c)** and **Figure 8(e)**, the TEM bright-field images of the microstructure in the as-stamped part are shown for three levels of deformation determined by Feritscope measurements. Through

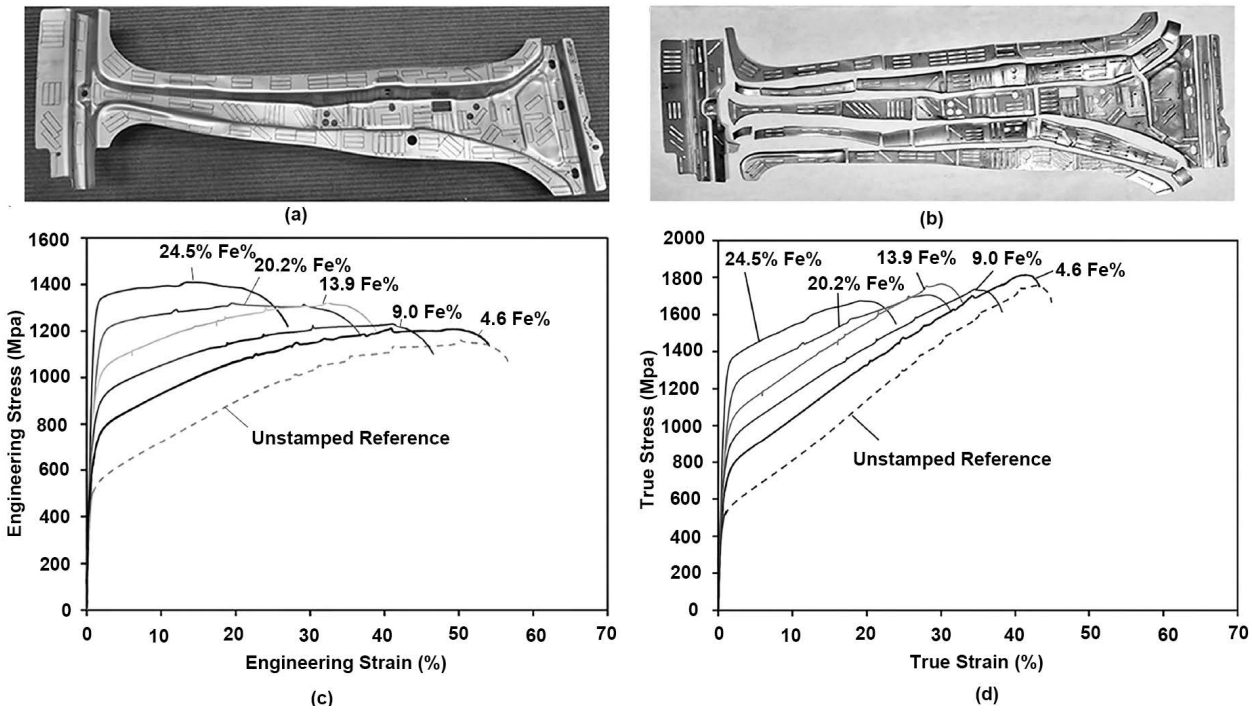

Figure 7. Tensile testing of specimens cut from the stamped B-pillar; (a) a view of the B-pillar with marked specimen positions, (b) a view of the B-pillar after specimen cutting, (c) stress-strain curve examples for specimens cut from the B-pillar with various level of magnetic phases volume percent (Fe%), and (d) corresponding true stress-true strain curve examples for specimens cut from the B-pillar with various level of magnetic phases volume percent (Fe%).

Table 1. Tensile properties of selected specimens.

Fe%	0.2% Yield Strength (MPa)	0.5% Yield Strength (MPa)	Ultimate Tensile Strength (MPa)	Tensile Elongation (%)
Unstamped (<1%)	463	496	1188	56.6
1.3	591	664	1215	59.0
4.4	588	743	1253	51.2
4.6	503	652	1212	54.2
9.0	621	774	1231	46.7
13.9	716	896	1326	39.1
20.2	787	1007	1320	37.0
24.5	954	1229	1410	27.0

studying multiple locations of the stamped part, a clear correlation is found with increases of Fe% in the samples and the amount of activated NR&S occurring during stamping.

In **Figure 8(a)**, the microstructure of the sample (with 4.6% Fe) is only slightly deformed. The grain boundaries are still clearly visible since the material transformation is limited as indicated by the small change in Fe% (*i.e.* from <1% to 4.6%). In **Figure 8(c)** and **Figure 8(e)**, TEM images show an increase in the volume percent of Microconstituent 1 in agreement with the Feritscope

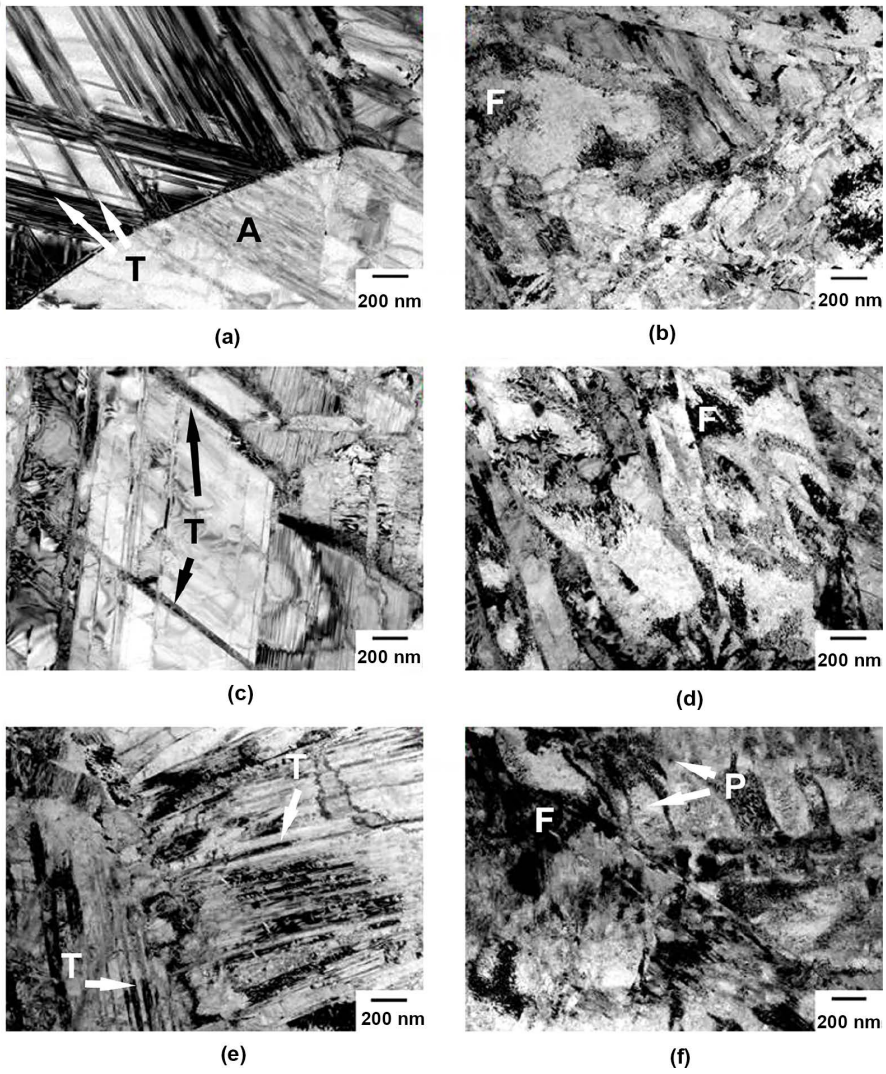

Figure 8. Bright-field TEM micrographs of the microstructure in specimens cut from the stamped B-pillar; (a) 4.6 Fe% sample before tensile deformation, (b) 4.6 Fe% sample after tensile deformation, (c) 13.9 Fe% sample before tensile deformation, (d) 13.9 Fe% sample after tensile deformation, (e) 24.5 Fe% sample before tensile deformation, (f) 24.5 Fe% sample after tensile deformation. On the micrograps, "T" represents twin, "P" represents precipitates, "A" represents austenite phase, and "F" represents ferrite phase.

measurements showing 13.9 and 24.5 Fe%, respectively. Higher dislocation density can be noted within the grains with increasing Fe% values. Twins are present in all three microstructures.

Additional TEM analysis of the microstructure was also done in the gauge section of the corresponding samples tested in tension. After deformation, similar Fe% was measured in all three sample gauges that ranged from 38 to 43 Fe%. Bright-field TEM images are provided in **Figure 8(b)**, **Figure 8(d)** and **Figure 8(f)**. It can be seen that after testing to failure, the structures in all three samples are similar with formation of distinct Microconstituent 1 and 2 regions as a result of further structural transformation through the NR&S mechanism during tensile testing.

The structural analysis of the samples cut from the stamped part confirms that the NR&S mechanism observed in laboratory samples during tensile testing as described in the Background section is also occurring during stamping operations. The NR&S mechanism is complex in nature [17] and specific structural changes will depend on the deformation pathway, localized strain state (*i.e.* uniaxial, biaxial, triaxial etc.), and strain rate. The destructive tensile testing was done to provide a holistic picture of the localized structure and property changes occurring during the stamping of the B-pillar. The measured tensile properties were correlated to structural changes during stamping depicted by Feritscope and HRc measurements of the tensile samples after cutting from the B-pillar prior to testing.

3.4. Non-Destructive/Destructive Property Correlations

Using the dataset of tensile properties measured from the destructive testing of the B-pillar, correlations of the measured tensile data can be made with both Rockwell C hardness and Feritscope measurements. With increasing hardness and magnetic phases volume percent (Fe%), both the yield and ultimate tensile strength are found to increase commensurate with reductions in elongationwhich is related to phase changes in the material during stamping. These phase changes depend on the level of straining leading to variable values of measured properties. The Pearson correlation coefficient (ρ) was calculated for yield strength (0.2% and 0.5% offset), ultimate tensile strength, and elongation, respectively, as a function of both hardness and magnetic phases volume percent (Fe%). Plots are provided in **Figure 9** for hardness and **Figure 10** for magnetic phases volume percent (Fe%). The calculated Pearson correlation between the compared measurements is noted above each subfigure.

For hardness the absolute value of the Pearson correlation coefficient ($|\rho|$) varies from 0.72 to 0.87, indicating moderate to strong linear correlations between these measurements. The absolute value of the Pearson correlation coefficient ($|\rho|$) for magnetic phases volume percent (Fe%) ranges from 0.78 to 0.91, indicating a moderate to strong linear correlation and one that is slightly stronger than for the hardness measurements. Based on the strength of these correlations, a linear model for predicting yield strength, ultimate tensile strength, and elongation can be created using hardness or magnetic phases volume percent.

3.5. Estimation of Properties in B-Pillar Stamping

Through non-destructive evaluation, a maximum value of 31 Fe% was measured in highly deformed areas of the B-pillar. Due to the physical limitations in cutting of tensile specimens in these areas, the maximum Fe% observed in the cut tensile specimens was 24.5%. Using established correlations based on ~200 data points and linear model described above, yield and tensile strength as well as total elongation were strength the tensile properties were estimated by extrapolation of the linear relationships to 31 Fe% as shown in **Figure 11(a)** and

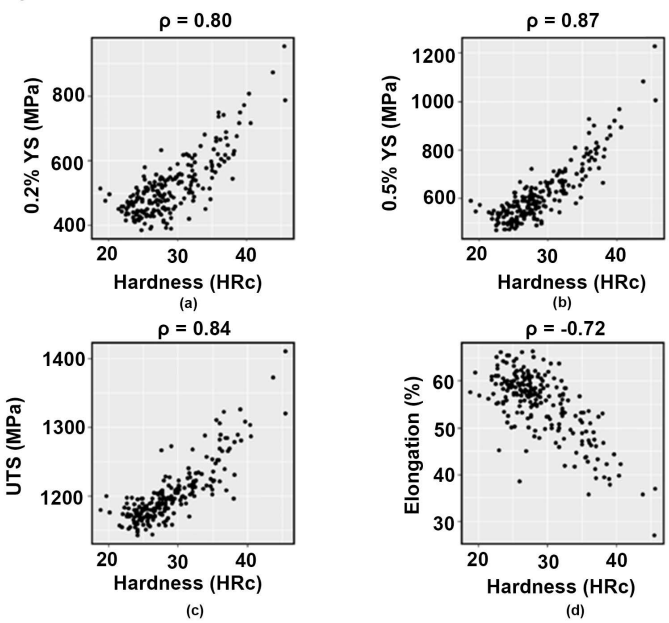

Figure 9. Linear correlation between hardness and (a) 0.2% offset yield strength, (b) 0.5% offset yield strength, (c) ultimate tensile strength, and (d) tensile elongation for the NXG™ 1200 B-pillar.

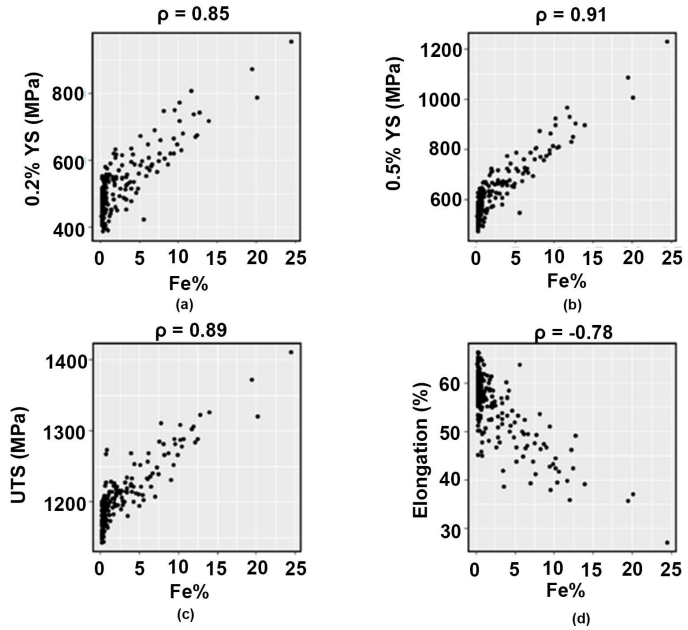

Figure 10. Linear correlation between magnetic phases volume percent (Fe%) and (a) 0.2% offset yield strength, (b) 0.5% offset yield strength, (c) ultimate tensile strength, and (d) tensile elongation for the NXG™ 1200 B-pillar.

Figure 11(b). The estimated tensile properties concurrent with the maximum amount of deformation were found to be at 1085 MPa for yield strength with 0.2% offset, at 1400 MPa for yield strength wit 0.5% offset, at 1490 MPa for ultimate tensile strength and at 15% for total elongation. Interestingly, the retained

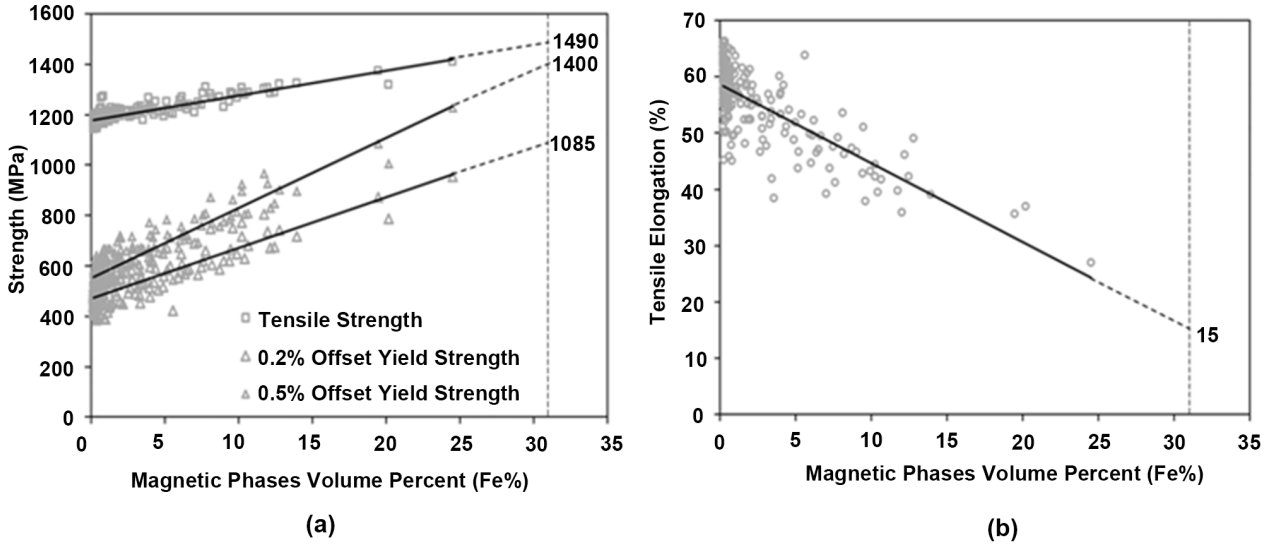

Figure 11. Extrapolation of tensile properties based on correlation with Feritscope; (a) strength properties extended to the maximum 31 Fe% found from non-destructive Feritscope measurements prior to cutting, (b) elongation extended to the maximum 31 Fe%.

ductility in the most deformed areas of the B-pillar after stamping is similar to other grades of AHSS in their respective undeformed, pre-stamped conditions. In addition to showing the level of strengthening achieved in the stamping, these results indicate that the material has a potential for applications requiring stamping of even more complex geometries and the resulting stamped parts retain capability for high energy absorption.

As shown above, a detailed analysis of property changes in the NanoSteel alloy sheet after stamping was performed on the B-pillar. The correlations of the tensile properties with the Feritscope measurements were found to be good with coefficient of determination or R2 from 60.2% to 83.7% as shown in **Figure 10**. This agrees well with the microstructural analysis whereby samples cut from the B-pillar with different amounts of localized strain developed structures similar to those found in tensile specimen gauges after testing. As understanding grows, the goal would be to develop predictive models of the material behavior in stamped parts through non-destructive testing. Ultimately, this will provide auto designers freedom to design complex geometries to take advantage of the unique NR&S deformation and strengthening mechanisms in metal stampings.

4. Conclusions

Bulk and local formability was demonstrated in the 3rd Generation NanoSteel NXG™ 1200 material by a number of laboratory tests including hole expansion, biaxial bulge, cup drawing, and guided bend testing. The extension of these test predictions for cold formability in an industrial process was confirmed by commercial stamping of the material into B-pillars at ambient conditions. A detailed analysis of the stamped parts revealed variations in structural changes and strengthening of the material after stamping depending on the localized defor-

mation applied in relation to the part geometry. The effect of the NR&S mechanism occurring in the areas of the B-pillar during forming has been quantified by using magnetic phases volume percent measurement coupled with tensile testing of the specimens cut from the stamped part.

The measured magnetic phases volume percent, yield strength, and ultimate tensile strength are shown to increase with increasing deformation level during forming especially in the areas of extensive bending and stretching with correlation to microstructural changes from the NR&S mechanism. Yield strengths (0.2% offset) up to 1085 MPa and tensile strengths up to 1490 MPa were estimated to be achieved in the stamped B-pillar while retaining a minimum of 15% estimated elongation. Initial correlation studies have demonstrated a capability to relate non-destructive evaluation methods with actual measured properties to develop a holistic picture of the structure and properties produced during stamping allowing for subsequent more detailed modeling and analysis. The developed correlations allowed estimation of properties in the areas where direct measurement are not available showing, in some locations, even higher strengthening effect from the NR&S mechanism. In the future, work will continue to understand the details of this 3rd Generation AHSS performance during industrial stamping operations as well as to correlate resulting properties in the stamped part with specific localized deformation conditions.

References

[1] Steel Market Development Institute (2014) Steel Is the Solution to Achieve 54.5 MPG by 2025. http://www.autosteel.org/research/growth-of-ahss.aspx

[2] Schaeffler, D.J. (2004) Introduction to Advanced High-Strength Steels—Part I, Grade Overview. *Stamping Journal*. https://www.thefabricator.com/

[3] Galán, J., Samek, L., Verleysen, P., Verbeken, K. and Houbaert, Y. (2012) Advanced High Strength Steels for Automotive Industry. *Revista de Metalurgia*, **48**, 118-131. https://doi.org/10.3989/revmetalm.1158

[4] Demeri, M.Y. (2013) Advanced High-Strength Steels—Science, Technology, and Application. *ASM International*.

[5] Baluch, N., Udin, Z.M. and Abdullah, C.S. (2014) Advanced High Strength Steel in Auto Industry: An Overview. *Engineering, Technology & Applied Science Research*, **4**, 686-689.

[6] Billur, E and Altan, T. (2010) Challenges in Forming Advanced High Strength Steels, Engineering Research Center for Net Shape Manufacturing (ERC/NSM), 285-334. http://www.ercnsm.org/

[7] Irie, T., Satoh, S. and Hashiguchi, K. (1981) Metallurgical Factors Affecting the Formability of Cold-Rolled High Strength Steel Sheets. *Transactions ISIJ*, **21**, 793-801.

[8] Schaeffler, D.J. (2005) Introduction to Advanced High-Strength Steels—Part II. *Processing Considerations*, September 13. https://www.thefabricator.com/article/metalsmaterials/introduction-to-advanced-high-strength-steels---part-i

[9] Schaeffler, D.J. (2017) The Importance of Local Formability When Working with AHSS.

https://www.thefabricator.com/article/stamping/the-importance-of-local-formability-when-working-with-ahss

[10] Advanced High Strength Steel (AHSS) Applications Guidelines V6.0 (2017), World Auto Steel, April 2017.

[11] Branagan, D.J., Sergueeva, A.V., Cheng, S., *et al.* (2013) Strategies For Developing Bulk Materials NanoTechnology (BMN) Into Industrial Products. *Material Science and Technology*, **29**, 1193-1199. https://doi.org/10.1179/1743284712Y.0000000161

[12] Branagan, D.J., Frerichs, A.E., Meacham, B.E., Ma, L., Yakubtsov, I.A., Cheng, S. and Sergueeva, A.V. (2014) New Mechanisms, Enabling Structures, and Advanced Properties Resulting in a New Class of 3rd Generation AHSS Sheet. SAE Technical Paper 2014-01-0989.

[13] Branagan, D.J., Frerichs, A.E., Meacham, B.E., Cheng, S. and Sergueeva, A.V. (2016) Overcoming the Paradox of Strength and Ductility. SAE Technical Paper, 2016-01-0357.

[14] Branagan, D.J. (2016) Designing Third Generation Advanced High-Strength Steel For Demanding Automotive Applications. *Advanced Materials & Processes*, 22-24.

[15] Branagan, D.J., Parsons, C.S., Machrowicz, T.V., Frerichs, A.E., Meacham, B.E., Cheng, S. and Sergueeva, A.V. (2016) Launch of A New Class of 3rd Generation Cold Formable AHSS, *Great Design in Steel 2016*, Laurel Manor Conference Center; Livonia, MI, 11 May 2016.

[16] ASTM E8/E8M-16a (2016) Standard Test Methods for Tension Testing of Metallic Materials. ASTM International, West Conshohocken. http://www.astm.org

[17] Branagan, D.J., Frerichs, A.E., Meacham, B.E., Cheng, S. and Sergueeva, A.V. (2017) 3rd Generation AHSS: Nanophase Refinement and Strengthening during Cold Deformation. *AIST International Symposium on New Developments in Advanced High-Strength Sheet Steels*, Keystone, 30 May-2 June 2017, 281-291.

[18] Branagan, D.J., Frerichs, A.E., Meacham, B.E., Cheng, S. and Sergueeva, A.V. (2016) 3rd Generation AHSS: Mechanisms Enabling High Cold Formability, Invited Talk. *MS&T* 2016, Salt Lake City, 24-27 October 2016.

[19] Kuhlman, S.J.H., Machrowicz, T.V., Parsons, C.S., Sergueeva, A.V., Frerichs, A.E., Meacham, B.E., Cheng, S. and Branagan, D.J. (2017) 3rd Generation AHSS High Strain Rate Tensile Testing. *MS&T* 2017, Pittsburg, 11 October 2017.

[20] Sergueeva, A.V., Frerichs, A.E., Meacham, B.E., Cheng, S. and Branagan, D.J. (2016) 3rd Generation AHSS: Pathway to Delayed Cracking Resistance. *MS&T* 2016, Salt Lake City, 24-27 October 2016.

[21] Machrowicz, T., Sergueeva, A., Bossert, E., Peterson, A. and Branagan, D. (2014) Understanding the Challenges and Uses of the 3rd Generation of Advanced High Strength Steels. http://bodyandassembly.com

[22] Frerichs, A.E., Meacham, B.E., Cheng, S., Sergueeva, A.V. and Branagan, D.J. (2016) 3rd Generation AHSS: Global vs. Local Formability. *MS&T* 2016, Salt Lake City, 24-27 October.

[23] Branagan, D.J., Frerichs, A.E., Meacham, B.E., Cheng, S. and Sergueeva, A.V. (2017) New Mechanisms Governing Local Formability in 3rd Generation AHSS. SAE Technical Paper. https://doi.org/10.4271/2017-01-1704

[24] Sergueeva, A.V., Frerichs, A.E., Meacham, B.E., Cheng, S. and Branagan, D.J. (2017) 3rd Generation AHSS: New Factors Affecting Local Formability. *International Symposium on New Developments in Advanced High-Strength Sheet Steels*, Keystone, 30 May-2 June 2017, 9.

[25] Justice, G.G., Sergueeva, A.V., Frerichs, A.E., Meacham, B.E., Cheng, S. and Branagan, D.J. (2018) Specimen Size Effect on Measured Tensile Properties Using Modern Full Range Extensometers. *Journal of Testing and Evaluation*.